RESEARCH ARTICLE
SOLID EARTH: GEODYNAMICS

Earth and Planetary Physics
10: 1–12, 2026
doi: 10.26464/epp2026016

Detecting the signal cycle of the deep Earth's dynamic processes based on GRACE satellite and CHAOS-7 model data

YongGang Zhang, ZhengTao Wang*, GangHua Ni, and ShiZe Zhang

School of Geodesy and Geomatics, Wuhan University, Wuhan 430072, China

Key Points:

- The main purpose of this study is to separate the core mass transfer contributions in GRACE global gravity data combined with various global hydrological models.
- The correlation analysis between the main principal components of core magnetic and gravity signals reveals that the trend in changes in the second-order time derivative of the core magnetic field coincide with those in the gravity field.
- Rapid changes have been observed since 2014 in the second temporal mode of the gravity field and the first temporal mode of the magnetic field.

Citation: Zhang, Y. G., Wang, Z. T., Ni, G. H., and Zhang, S. Z. (2026). Detecting the signal cycle of the deep Earth's dynamic processes based on GRACE satellite and CHAOS-7 model data. *Earth Planet. Phys.*, *10*(1), 1–12. http://doi.org/10.26464/epp2026016

Abstract: The GRACE (Gravity Recovery and Climate Experiment) space mission recorded temporal variation characteristics of the global gravity field at decadal timescales. The gravity data have been shown to capture the dynamics of flows within the outer core and their effects on the core–mantle boundary. We first aim to remove global surface process gravity signals from the GRACE data. We then construct the global core magnetic field according to the CHAOS-7 model. Finally, we apply the blind source separation method to decompose the processed gravity signals and core magnetic signals and compute the power spectral density of the gravity and magnetic field signals by using the Lomb–Scargle periodogram approach. We have discovered a signal cycle (of ~6 years) in the principal components of the core magnetic and gravity signals, potentially as a result of deep Earth processes. The main principal components of the core magnetic and gravity signals reveal that the variation trends in the second-order time derivative of the core magnetic field are similar to those in the gravity field. After 2014, the second-order time derivative of the core magnetic field exhibited linear and rapid change characteristics, which were the same as the change in the gravity field and are consistent with existing research results.

Keywords: GRACE satellite; time-variable gravity field; core magnetic field; mass transport; blind source separation method

1. Introduction

Before the launch of gravity satellites, our knowledge of the Earth's gravity field was limited to the static part, with only a relatively accurate understanding of its temporal variation up to its lower spherical harmonic order. However, the situation drastically improved with the gravity satellite missions (e.g., the GRACE [Gravity Recovery and Climate Experiment] mission in 2002, followed by its successor GRACE-FO mission in 2018 [Chen JL, 2019]; the CHAMP mission [Challenging Minisatellite Payload] in 2000; and the GOCE mission [Gravity field and steady-state Ocean Circulation Explorer] in 2009 [Wahr, 2007; Tapley et al., 2019]). The gravity satellite missions have revolutionized our understanding of the dynamic processes of the planet's gravity field.

Changes in the Earth's gravity field over years and decades seem to be primarily driven by variations in land water storage and ocean mass. Seasonally, however, a notable discrepancy exists between the expected results and actual observations (Dumberry and Mandea, 2022). Some of these observed changes are the result of surface processes. The flow in the Earth's liquid core can also affect changes in the Earth's gravity field on interannual to decadal timescales, so some unexplained signals may also be related to the core flow (Dumberry, 2010). The mass redistribution caused by the dynamic process of the Earth's fluid core mainly causes gravity changes in different ways, such as density anomalies leading to convection on the outer core surface of the fluid; vertical motion in density layers that generates density migration; pressure changes caused by core flow over time affecting the topography of the core–mantle boundary (CMB); and elastic deformations resulting from the processes mentioned (Merriam, 1988; Fang M et al., 1996; Dumberry and Bloxham, 2004).

Recently, several studies have indicated that the geophysical field signals derived from space geodetic measurements may be related to processes of core dynamics occurring at the CMB (Mandea et al., 2020). Researchers have confirmed that the dominant spatiotemporal modes of time-varying gravity field changes recorded by satellites are closely related to the dominant

First author: Y. G. Zhang, zhangyonggang20@whu.edu.cn
Correspondence to: Z. T. Wang, ztwang@whu.edu.cn
Received 03 JUL 2025; Accepted 31 OCT 2025.
First Published online 21 NOV 2025.

spatiotemporal modes of the second-order time derivative of the radial component of the core magnetic field after correcting for the surface process effects (Mandea et al., 2012). This research covers the time span from 2002 to 2010, and subsequent research has shown a strong correlation between secular acceleration (second-order time derivative) of the radial component of the core magnetic field and the residual gravity signal at several geographic locations (Mandea et al., 2020). Recently published research studies have indicated recurring variations in several Earth systems approximately every 6 years, and some of these 6-year cycle changes have resulted from the Earth's deep dynamic processes at the CMB (e.g., for length of day; Ding H and Chao BF, 2018; Watkins et al., 2018; Chen JL et al., 2019; Chao BF et al., 2020; Pfeffer et al., 2023). Researchers have found that the time-varying convective fluctuations in the density structure of the outer core influence Earth's gravity field and have provided predictions of its variations over the past century (Dumberry, 2010). These researchers have examined the mechanisms behind various core processes, discussed methods for reconstructing gravity changes and ground deformations, and outlined approaches to estimate their amplitudes (Dumberry and Mandea, 2022). A spatiotemporal correlation between the gravity and magnetic fields has been attributed to physicochemical processes, called the dissolution–crystallization model, at the CMB (Mandea et al., 2012, 2015). These processes could potentially cause more significant perturbations in the surface gravity field (Mandea et al., 2015) compared with those considered by Dumberry (2010) and Rosat et al. (2021). Several statistical methods, such as joint singular value decomposition (SVD) and multivariate singular spectrum analysis (MSSA), have been used to identify similar patterns between Earth's gravity and magnetic fields, and the researchers have found the oscillations in Earth's gravity and magnetic field signals with cycles spanning approximately 6 to 7 years (Saraswati et al., 2023).

In the studies mentioned, researchers believe that the dynamic processes in the Earth's core are the source of the observed geophysical field signals, which indicates that geodetic observations can be used to study the dynamic processes within the Earth's core. Although numerous scientific papers have been published in recent years that are focused on surface mass redistributions based on GRACE data, only a limited number of studies have focused on mass redistributions in the deep Earth (Mandea et al., 2020; Fok and Ma ZT, 2021). The main purpose of this study is to separate the core mass transfer contributions in GRACE global gravity data combined with various hydrological models. In Section 2, we analyze and include various surface hydrological models required for our research. On the basis of GRACE gravity field data, we use the hydrological models to obtain residual gravity series containing signals from the Earth's core after removing various noncore signals. We next compute the second-order time derivative of the core magnetic field based on the CHAOS-7 model. Blind source separation (BSS) methods are applied to process the gravity and magnetic field signals to obtain their spatial and temporal modes. We briefly introduce the computational methods involved in the research in Section 3. We then present the results of our research in Section 4. We find that the dominant principal components (PCs) of the gravity signal correlate well with the dominant PCs of the magnetic field signal. Both fields have presented rapid linear changes since 2014. We compute and compare the power spectral density (PSD) of the gravity and magnetic field signals. Finally, in Section 5, we discuss the characteristics of similar modes and conclude, based on the existing research results, that the processed gravity field signals result from the mass transfer processes of the Earth's deep interior.

2. Data

2.1 GRACE Data

The GRACE gravity field data are publicly available and are mainly released by three institutions. We use the GRACE/GRACE-FO RL06 Mascon Solutions provided by the Center for Space Research (CSR, The University of Texas at Austin, Center for Space Research; Save et al., 2016). During data processing, the CSR has removed tidal effects (Bettadpur, 2007; Dahle et al., 2012; Save et al., 2016). The 60-degree model provided by the CSR is used in this study. The published GRACE spherical harmonic coefficient solution is converted to grid mass anomalies according to the method described in the GRACE CSR User Handbook (Wahr et al., 1998), and postprocessing includes (1) adding independent estimates of the Earth's mass motion center and the Earth's oblateness based on satellite laser ranging data (C_{20} correction); (2) filtering related errors characterized by north–south stripes; and (3) correcting the glacial isostatic adjustment (GIA correction) based on the ICE6G-D model (Purcell et al., 2016).

To separate the time-variable deep Earth signal from the GRACE gravity data, we use the corresponding hydrological model for each contribution (e.g., the atmosphere, oceans, ice sheets, glaciers, and land water) and remove the signal from the GRACE gravity fields. Hereafter, we refer to relevant references and introduce various hydrological datasets used in our research, and we list all acronyms, full names, and characteristics of various models used to correct the GRACE data in Table 1 of Section 4 (Lecomte et al., 2023).

2.2 Global Land Data Assimilation System (GLDAS) Hydrological Model

The National Aeronautics and Space Administration (NASA) releases the GLDAS model in collaboration with the National Centers for Environmental Prediction in the United States. This model uses multi-source data and advanced data processing techniques to obtain changes in surface fluid on the land, and it outputs various physical parameters of the land surface. This new land surface modeling system combines data from advanced observation systems to improve enhanced research in hydrometeorology (Rodell et al., 2004).

In this study, we choose the GLDAS-Noah model. The overall land water storage anomaly (soil moisture, root zone water, vegetation water, runoff, canopy water, surface snow, etc.) is synthesized and normalized into the equivalent water height format as the GRACE data and used to subtract the land water storage component from the GRACE signal.

Table 1. Abbreviations, full names, and characteristics of the various models used to correct the GRACE data.

Model (Abbreviations)	Model (Full name)	Component
GRACE	Gravity Recovery and Climate Experiment	Raw total signal
AOD1B	Atmosphere and Ocean De-aliasing Level-1B	Atmospheric loading and associated ocean bottom pressure
GLDAS	Global Land Data Assimilation System	Land water storage
ECCO	Estimating the Circulation and Climate of the Ocean	Sea level anomaly data
WOA	World Ocean Atlas	Ocean temperature and salinity data
ICE6G-D	ICE6G-D	Glacial isostatic adjustment (GIA)
RACMO	Regional Atmospheric Climate Model	Land ice data

2.3 Estimating the Circulation and Climate of the Ocean (ECCO) Oceanic Hydrologic Model

The ECCO consortium was established in 1999, with a primary focus on conducting detailed research in the fields of ocean circulation and climate. The solutions combine the ocean circulation models with the global ocean datasets. Today, with continuous support from NASA's Physical Oceanography and Sea Ice Modeling Building Blocks program, ECCO is working to improve the scope and accuracy of ocean state estimations. Unlike typical data assimilation (such as that used in numerical climate prediction), ECCO provides a consistent estimation of the physical characteristics of the ocean over time. The long-term goal of ECCO is to provide a global high-resolution state estimate coupled with ocean, sea ice, biogeochemistry, and atmosphere (Forget et al., 2015).

In this study, we choose the ECCO Version 4, Release 4 product, which combines the Massachusetts Institute of Technology (MIT) general circulation model (MITgcm) and most available satellite and *in situ* data to generate a physically consistent estimate of the water cycle in the ocean. The sea level anomaly (SLA) data from the ECCO product is selected to remove the signal of ocean mass variations.

2.4 World Ocean Atlas (WOA) Dataset

The global SLA changes contain the steric variations and the mass variations, so we need to compute the steric sea level (SSL) to determine the mass change of the ocean (Chen JL et al., 2005; Chambers, 2006). The World Ocean Atlas 2018 (WOA2018) is funded by the National Oceanic and Atmospheric Administration and managed by the National Centers for Environmental Information (NCEI). Its purpose is to compile an oceanographic database and to perform objective analyses and diagnostic studies based on this database. The data in this atlas are derived from profile measurements in the World Ocean Database 2018 (WOD2018), which is compiled and objectively analyzed by the NCEI online. We choose WOA2018 released in July 2019 in our study, and the dataset is updated from previous versions of the WOA.

2.5 ICE6G-D Model

The currently available global GIA models include ICE-3G, ICE-4G (VM2), ICE-5G (VM2), and ICE-6G_C (VM5a), as well as the Paulson07 and Geruo13 models. As for regional GIA models, they mainly focus on the Antarctic region, such as the IJ05, IJ05_R2, W12, and W12a models.

Recently, the University of Toronto released a new GIA model based on the ICE-NG (VMX) sequence, called ICE-6G_C (VM5a). Initially released in the form of spherical harmonic coefficients up to degree 256, it has been demonstrated to provide accurate data fitting for global positioning system (GPS) observation databases, time-variable gravity field data obtained from GRACE satellite inversion, and relative sea level histories determined by radiocarbon dating from North America, Eurasia, and Antarctica. The studies suggested that it was possible to improve the ICE-6G_C model and proposed the ICE-6G_D model, which improved the previous model results to some extent but still had some differences at the physical layer (Purcell et al., 2016).

2.6 Regional Atmospheric Climate Model (RACMO) Model

The High-Resolution Limited Area Model (HIRLAM) is a weather forecasting model with high resolution for limited regions. In 1993, the Institute for Marine and Atmospheric Research Utrecht assumed control and improved the model to better represent extreme conditions on glacier surfaces, and they began to release the RACMO model.

The second version of RACMO combines the dynamic core of the HIRLAM and the Integrated Forecasting System physics module. Because of the rapid development of computing power, recent updates of RACMO are applied not only to the Antarctic and Greenland ice sheets but also to smaller regions, such as Dronning Maud Land and Patagonia, with higher resolution. The RACMO2.4 model has now been released (van Dalum et al., 2024).

2.7 CHAOS-7 Magnetic Field Data

The geomagnetic field, as measured by satellites and ground-based observatories, originates from both internal and external sources of the Earth. Internal sources comprise the dynamo process in the liquid outer core and crustal magnetization in the Earth's upper layers, whereas external sources are electrical currents within the ionosphere and magnetosphere (Mandea et al., 2020).

The National Space Institute at the Technical University of Denmark released the CHAOS-7 model, a time-dependent near-Earth geomagnetic field model covering the period from 1999 to 2020. This model relies on magnetic field data from low Earth orbit satellites, along with annual differences derived from the monthly averages of ground observatory measurements. The

CHAOS-7 model includes a time-varying core field up to degree 20, a static internal field up to degree 25 combined with the LCS-1 (lithospheric field model 1 derived from CHAMP and Swarm satellite data), a model of the magnetospheric field with its corresponding induced field, and the necessary satellite parameters for computation (Olsen et al., 2006, 2017, 2020; Finlay et al., 2020).

In our study, we construct the core magnetic field model based on CHAOS-7 model data and compute the second-order time derivative of the radial component of the core magnetic field based on 6-degree B-spline interpolation.

3. Methods

3.1 GRACE Gravity Field

We use the spherical harmonic coefficients of the GRACE monthly Earth gravity field data to compute the global mass changes in equivalent water height by an inversion method proposed by Wahr et al. (1998):

$$h(\theta,\lambda) = \frac{R\rho_{ave}}{3\rho_w}\sum_{l=0}^{l_{gra}}\sum_{m=0}^{l}\bar{P}_{lm}(\cos\theta)\frac{2l+1}{1+k_l}\left(\Delta\bar{C}_{lm}\cos(m\lambda)+\Delta\bar{S}_{lm}\sin(m\lambda)\right). \quad (1)$$

The equation above is the basic formula for computing the global mass transfer change using GRACE data, where R = 6371.2 km is the Earth's mean reference radius; (θ, λ) are spherical polar coordinates; l_{gra} is the maximum degree and order of the GRACE gravity field expansion; k_l is the elastic Love number of degree l; $\bar{P}_{lm}$ is the associated Legendre function; $\Delta\bar{C}_{lm}$ and $\Delta\bar{S}_{lm}$ are variations of the spherical harmonic coefficients; ρ_w is the density of water; and ρ_{ave} is the average density of the Earth.

When computing the global mass change grids, we apply the following postprocessing methods: (1) C_{20} correction, adding independent estimates of the Earth's center of mass motion and the Earth's oblateness based on satellite laser ranging data to replace the C_{20} coefficient in GRACE data; (2) Gaussian smoothing; (3) filtering related errors characterized by north–south stripes as features; (4) correcting the GIA; and (5) applying cubic spline interpolation to fill in the missing data (Wahr et al., 1998; Swenson and Wahr, 2002; Mandea et al., 2020). We compute the GRACE global time-varying gravity field equivalent water height in April 2002, as shown in Figure 1.

3.2 CHAOS-7 Magnetic Field

The vector magnetic field $\boldsymbol{B}$ can be represented by a scalar potential such that $\boldsymbol{B} = -\nabla V$, and the magnetic scalar potential $V = V^{ext} + V^{int}$ consists of internal sources and external sources (Finlay et al., 2020).

The internal parts of the CHAOS-7 model are represented as spherical harmonics. We focus on the core magnetic field and adopt a spherical harmonic expansion:

$$V(r,\theta,\lambda) = R\sum_{l=1}^{l_{int}}\sum_{m=0}^{l}\hat{P}_{lm}(\cos\theta)\left(\frac{R}{r}\right)^{l+1}\left(g_{lm}\cos(m\lambda)+h_{lm}\sin(m\lambda)\right), \quad (2)$$

where R = 6371.2 km is the Earth's mean radius; (r, θ, λ) are spherical polar coordinates; $\hat{P}_{lm}$ is the Schmidt seminormalized associated Legendre function; g_{lm}, h_{lm} are the Gauss coefficients; and l_{int} is the maximum degree and order of the core magnetic field expansion. We choose the coefficients (g_{lm}, h_{lm}) up to l_{int} = 20.

On the basis of 6-degree B-spline interpolation, we compute the second-order time derivative of the radial component of the core magnetic field in the global grids, whose resolution corresponds to the spatial and temporal resolution of global mass transfer change grids. The result of December 2015 is shown in Figure 2.

3.3 Computation of the Ocean Mass Change

When considering the impact of postglacial rebound (GIA correction), we compute the global ocean mass change in the equivalent water height, based on global SLA and SSL changes:

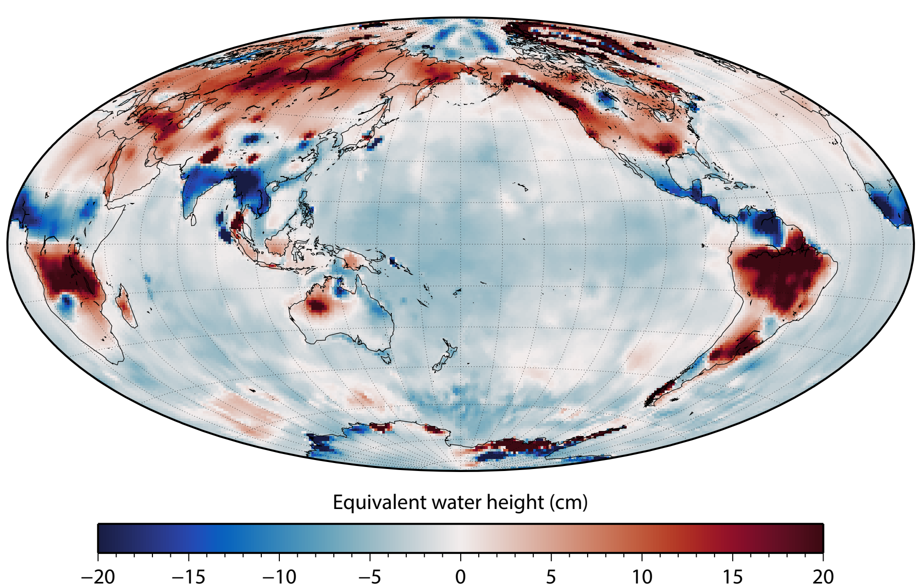

Figure 1. GRACE global time-varying gravity field equivalent water heights (April 2002).

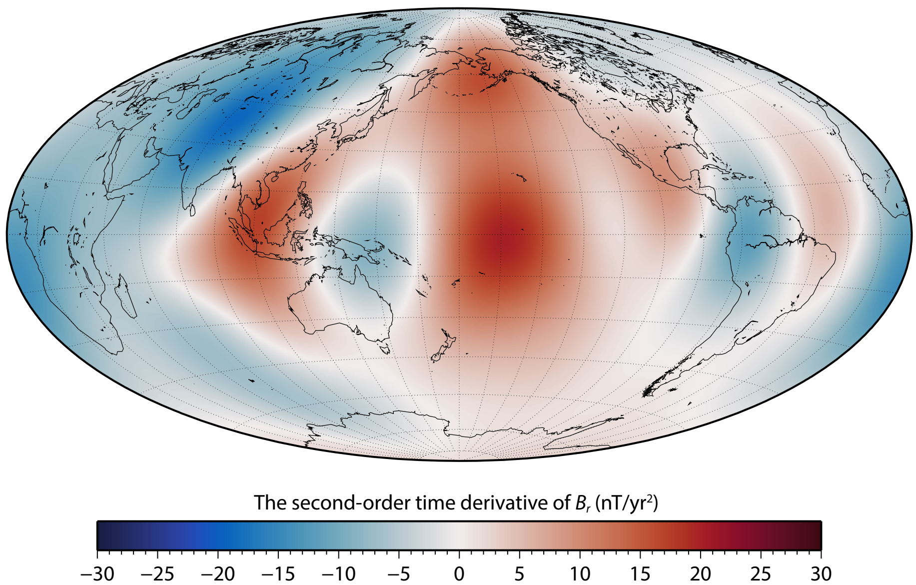

Figure 2. The second-order time derivative of the radial component of the core magnetic field in the global grids (December 2015).

$$\Delta\eta_{\mathrm{SSL}}(\theta,\lambda,t) = -\frac{1}{\rho_0}\int_{-h}^{0}[\rho(\theta,\lambda,t,z,S,T) - \bar{\rho}(\theta,\lambda,t,z,\bar{S},\bar{T})]\,\mathrm{d}z, \quad (3)$$

$$\mathrm{SLA}(\varphi,\lambda,t) = \Delta\eta_{\mathrm{SSL}}(\varphi,\lambda,t) + \Delta\mathrm{EWH}_{\mathrm{mass}}, \quad (4)$$

where SLA is Sea Level Anomaly; EWH is Equivalent Water Height; $\Delta\eta_{\mathrm{SSL}}$ is the steric sea level; (θ, λ) are spherical polar coordinates; h is the maximum depth; ρ_0 is the reference density (1027 kg/m^3); and the overbar indicates an average (computed in WOA2018, where T is temperature and S is salinity; Chen JL et al., 2005; Chambers, 2006).

3.4 Blind Source Separation Method

3.4.1 Principal components analysis

Before introducing the independent components analysis (ICA) method, we briefly introduce the principal components analysis (PCA) method. This method is also known as an empirical orthogonal function (EOF) analysis, which is a statistical decomposition method for analyzing the structural features in matrix data and extracting the main features of the data.

If one grid point is observed n times, then the observation vector $\boldsymbol{X}_i$ corresponding to this grid point can be represented as

$$\boldsymbol{X}_i^{\mathrm{T}} = \begin{pmatrix} x_{i,1} \\ x_{i,2} \\ \vdots \\ x_{i,n} \end{pmatrix}. \quad (5)$$

For m grid points, with each being measured n times, after removing the mean from each observation, time series are arranged row-wise in a matrix $\boldsymbol{Y}$ with dimensions of $m \times n$ $(m > n)$:

$$\boldsymbol{Y} = \begin{pmatrix} x_{1,1} & x_{1,2} & \cdots & x_{1,n} \\ x_{2,1} & x_{2,2} & \cdots & x_{2,n} \\ \vdots & \vdots & \ddots & \vdots \\ x_{m,1} & x_{m,2} & \cdots & x_{m,n} \end{pmatrix}. \quad (6)$$

The $m \times m$ signal covariance matrix $\boldsymbol{Q}$ contains the variances and covariances (i.e., second central moments) of the data viewed as time series per location. It can be estimated as

$$\boldsymbol{Q} = \frac{1}{n}\boldsymbol{Y}\boldsymbol{Y}^{\mathrm{T}}. \quad (7)$$

We use the SVD method to perform a statistical signal decomposition on the observation matrix in Equation (6) to study the spatiotemporal characteristics of the residual gravity signal and core magnetic signal after applying all corrections.

On the basis of the SVD decomposition, Equation (6) can be decomposed into the following form:

$$\boldsymbol{Y} = \boldsymbol{U}\boldsymbol{\Lambda}\boldsymbol{V}^{\mathrm{T}}, \quad (8)$$

where $\boldsymbol{U}$ is the eigenvector matrix of covariance matrix $\boldsymbol{Q}$; the eigenvectors are called EOFs, or spatial patterns; and $\boldsymbol{\Lambda}$ is the diagonal matrix $(m \times n)$ arranged in descending order. We take the first n rows of matrix $\boldsymbol{\Lambda}$ to form an $n \times n$ square matrix $\boldsymbol{\Lambda}'$, and the eigenvalues of the matrix $\boldsymbol{Q}$ are

$$\Delta = \boldsymbol{\Lambda}'\boldsymbol{\Lambda}'. \quad (9)$$

When computing the PCs, we take the normalization process. Empirical orthogonal functions constitute (normalized) spatial patterns whose amplitude evolution is given by the corresponding PCs:

$$\boldsymbol{P}^{\mathrm{T}} = \boldsymbol{U}^{\mathrm{T}}\boldsymbol{Y}\left(\sqrt{\frac{\Delta}{n}}\right)^{-1}, \quad (10)$$

$$\boldsymbol{E} = \boldsymbol{Y}\boldsymbol{P}\left(\boldsymbol{P}^{\mathrm{T}}\boldsymbol{P}\right)^{-1}, \quad (11)$$

where $\boldsymbol{P}$ is the matrix of PCs and $\boldsymbol{E}$ is the matrix of EOFs.

For the retained $r < n$ dominant spatial modes and corresponding r temporal modes after decomposition, the observation matrix can be approximately reconstructed by the following equation:

$$\boldsymbol{Y} \approx \boldsymbol{Y}_r = \boldsymbol{E}_r\boldsymbol{P}_r^{\mathrm{T}}, \quad (12)$$

where the dimensions of $\boldsymbol{E}_r$ and $\boldsymbol{P}_r$ are $m \times r$ and $n \times r$, respectively, and r is referred to as a "mode" of the observation matrix.

3.4.2 Independent components analysis

The PCA method described above is a second-order statistical decomposition method. In the decomposition process, whether based on the covariance matrix constructed from the time series or the correlation matrix, only second-order statistical information in the observed signal is included, and the higher order moments of the observed probability density function are ignored. Moreover, the different modes obtained through PCA decomposition only appear to be uncorrelated with each other, rather than independent.

To extend and improve traditional PCA methods, it is necessary to consider the higher order statistical information of the probability density function of the observed data during the decomposition process. Independent components analysis was proposed to incorporate the higher order statistical information of the probability density function into the decomposition process. The basic idea of ICA is to decompose the observed signal into multiple independent components by using higher order statistical information, with the aim of achieving independence among the decomposed components without prior information. It can be seen as an extension of the traditional PCA method based on second-order statistical information.

The problem of decomposing signals based on statistical information is generally formulated as finding a function f that transforms the observation matrix $\boldsymbol{Y}$ into a source signal matrix $\boldsymbol{S}$:

$$\boldsymbol{S} = f(\boldsymbol{Y}). \tag{13}$$

In most applications, the transformation relationship described above is simplified by assuming a linear transformation (the matrix $\boldsymbol{W}$). Therefore, the function transformation in the equation above can be expressed as

$$\boldsymbol{S} = \boldsymbol{W}\boldsymbol{Y}. \tag{14}$$

We also use the SVD method to perform statistical signal decomposition on the observation matrix in Equation (14). The ICA decomposition based on orthogonal mode rotation can be expressed as

$$\boldsymbol{Y} \approx \boldsymbol{Y}_r = \boldsymbol{E}_r\boldsymbol{R}_r\boldsymbol{R}_r^{\mathrm{T}}\boldsymbol{P}_r^{\mathrm{T}}, \tag{15}$$

where $\boldsymbol{P}_r$, $\boldsymbol{Y}_r$, $\boldsymbol{E}_r$ are the same as in Equation (12). The matrix $\boldsymbol{R}_r$ is a square matrix of dimensions $r \times r$. To obtain the ICA decomposition, it is necessary to determine this rotation matrix $\boldsymbol{R}_r$. Kusche et al. (2011) and Cardoso (1999) introduced a practical method for calculating the matrixes $\boldsymbol{R}_r$ and $\boldsymbol{W}$.

4. Results

In this section, we focus on the results from CSR GRACE/GRACE-FO RL06 Mascon Solutions and the CHAOS-7 model. To unify the period and resolution of various models, we analyze the monthly time-variable sequence of the GRACE gravity field and the CHAOS-7 core magnetic field from April 2002 to December 2015. The spatial resolution of both models is 1° × 1°. The other data sets are introduced in Section 2. For ease of reading, the CHAOS-7 core magnetic field is called the magnetic field and the GRACE gravity field is referred to as the gravity field. Because of the poor fit between the magnetic field model and ground observatory data in high-latitude regions (Finlay et al., 2020), the study area selected was in the middle- to low-latitude regions, ranging from −60° to 60°.

We first remove the surface process components, including atmospheric loading, terrestrial hydrological changes, land ice components, and oceanic mass changes caused by oceanic circulation changes from the gravity field. We then separately analyze the gravity and magnetic fields by ICA. Note that we present the spatial pattern as the time correlation coefficient between the PC of each mode (Saraswati et al., 2023). We also compute the PSD of individual time series with the Lomb–Scargle periodogram (VanderPlas, 2018).

4.1 Gravity Field Data Results

We have performed the ICA method on the gravity field. The PCs and spatial pattern of the first six leading modes are shown in Figure 3. The six modes account for 13.08%, 11.19%, 9.76%, 9.35%, 7.88%, and 4.30% of the total variance, respectively. We have calculated the PSD of each PC, as shown in Figure 4. The first and fourth modes exhibit distinct annual cycle characteristics and seasonal variations, which result from residual surface hydrological signals. In the analysis below, we focus on the remaining four modes reflecting long-period variations.

The second mode (Figure 3b) does not exhibit annual cycle behavior as clearly as do the first and fourth modes (Figures 3a and 3d), and it displays a relatively stable signal overall. After 2012, it shows the characteristic of a rapid linear change. A less prominent peak point is located near the 5-year period, as shown in Figure 4b. The significantly correlated regions of this mode are approximately located between longitude 0° and 40°E and in the South Atlantic Ocean. The third mode (Figure 3c) also presents the characteristic of long-period variation. Compared with the second mode, the third mode has a relatively prominent peak point at the 5.8-year period (Figure 4c), and its significantly correlated regions are located in Africa and the West Pacific Ocean. The fifth mode (Figures 3e and 4e) is dominated by a 10-year period, with the spatial extent scattered across the globe. The sixth mode (Figure 3f) is dominated by long-period variation like the third mode. The significantly correlated areas are scattered across the South Pacific Ocean and the Indian Ocean, and the peak appears at the 5.2-year period (Figure 4f).

4.2 Magnetic Field Data Results

We have performed the ICA method on the second-order time derivative (secular acceleration) of the magnetic field. The PCs and spatial pattern of the first six leading modes are shown in Figure 5. The six modes account for 20.54%, 17.98%, 16.04%, 15.57%, 13.89%, and 7.85% of the total variance, respectively. We have calculated the PSD associated with each PC of the magnetic field, as shown in Figure 6.

The first mode (Figure 6a), which captures 20.54% of the total variance, exhibits time variability with a period of T = 4.8 years and

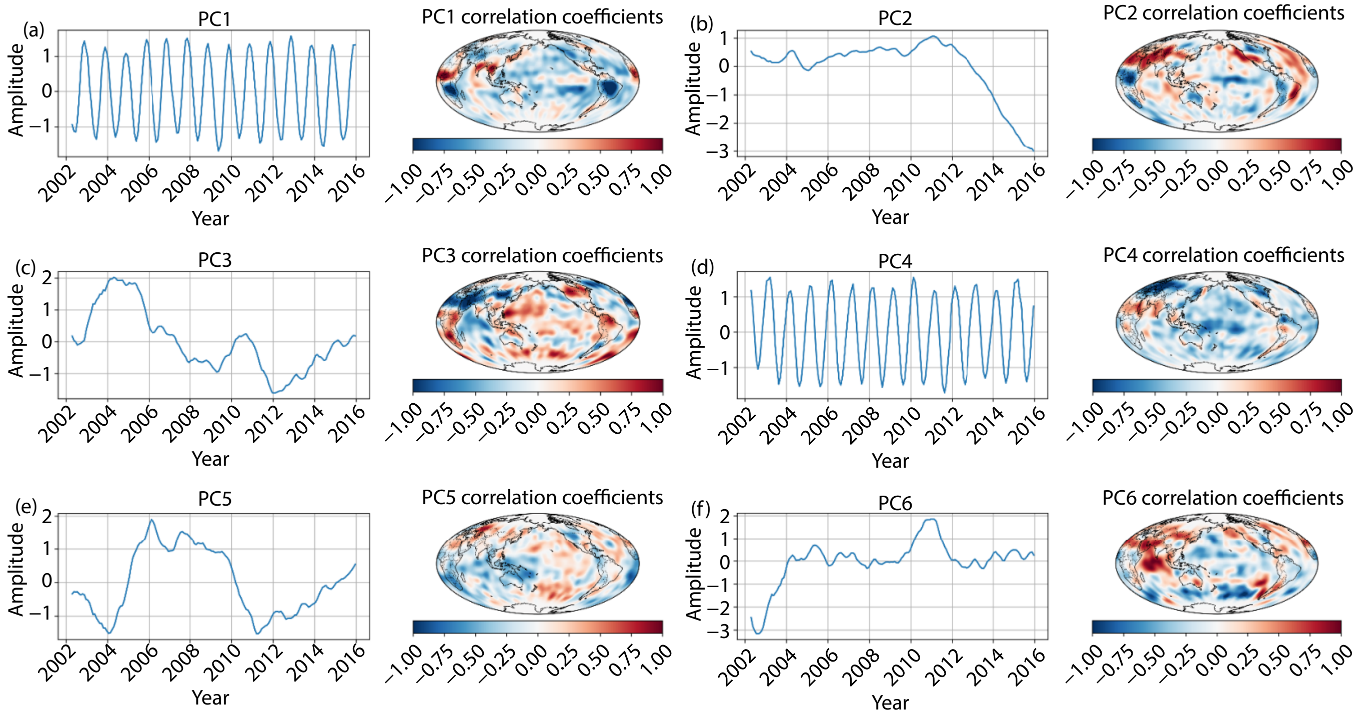

Figure 3. Principal components of the gravity field from the ICA and the correlation coefficients between their associated spatial patterns and the gravity field.

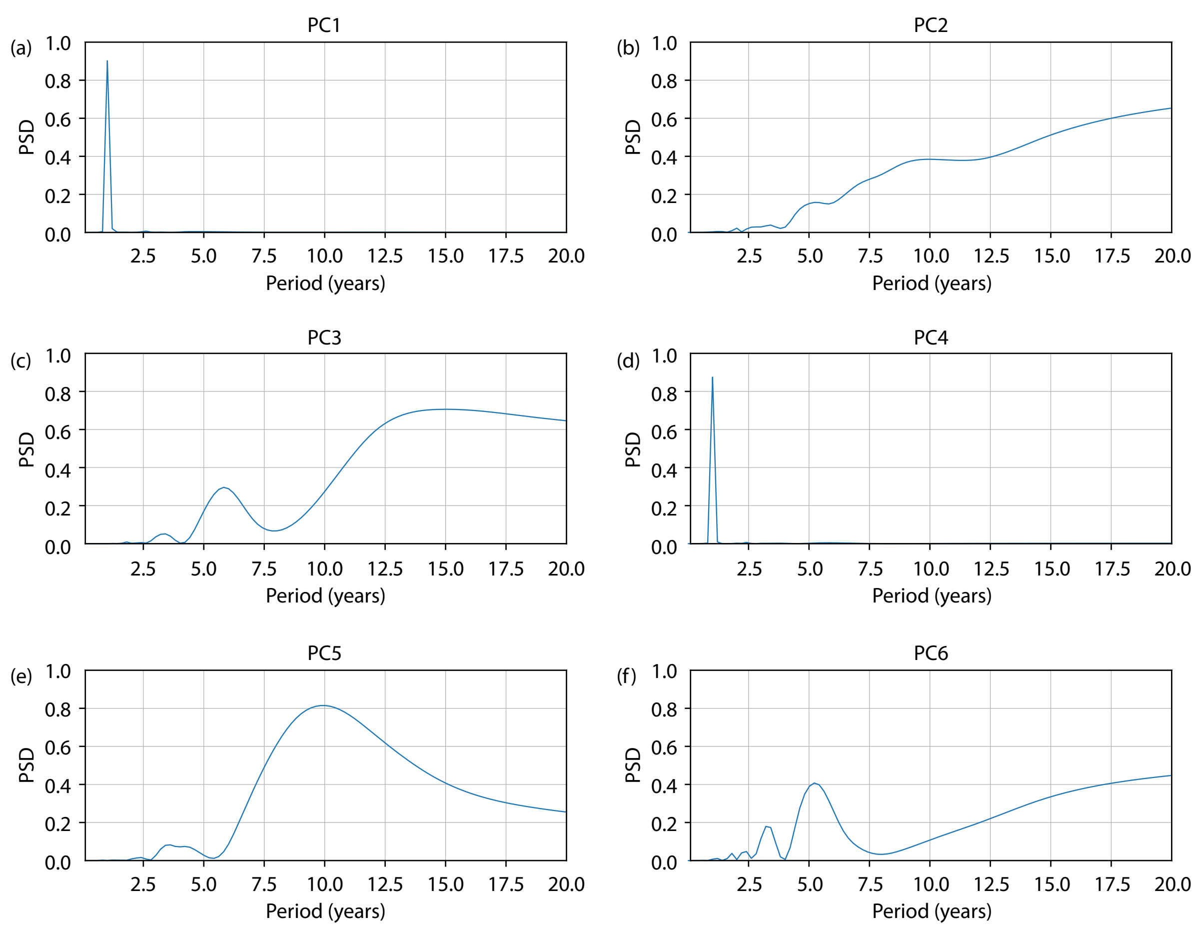

Figure 4. The PSD of each PC of the gravity field from the ICA.

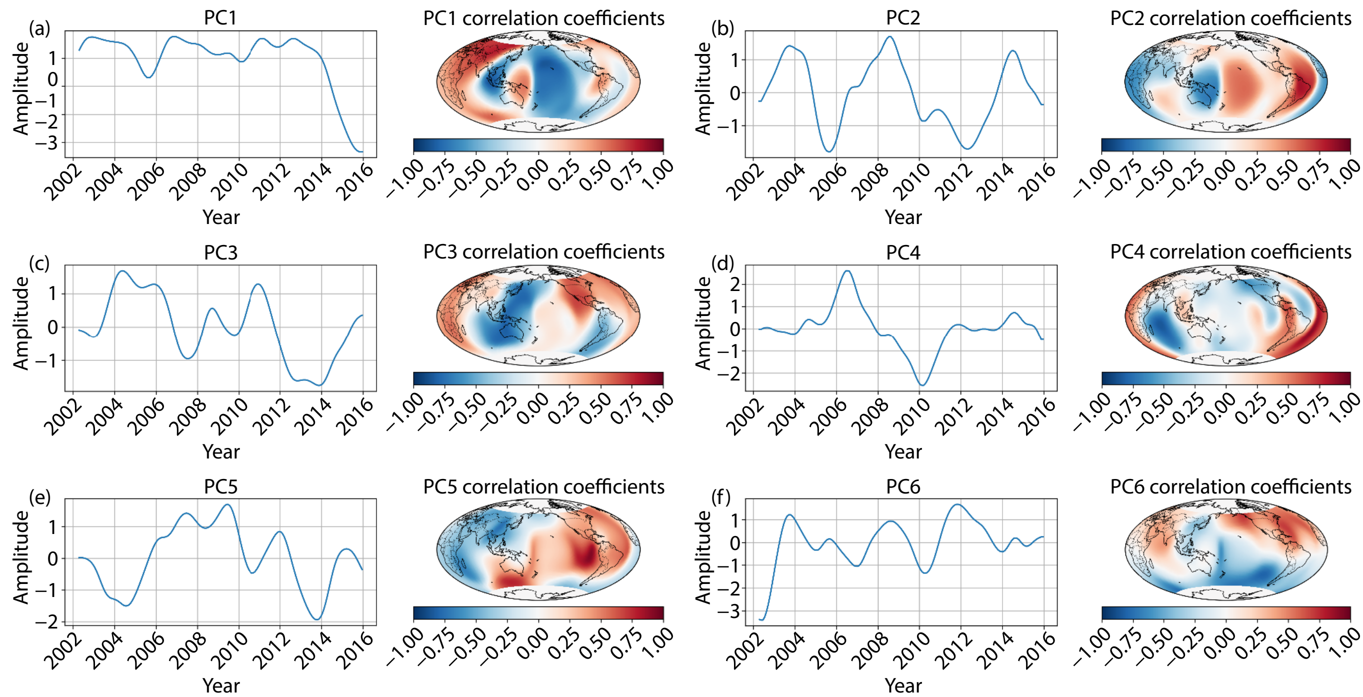

Figure 5. Principal components of the magnetic field from the ICA and the correlation coefficients between their associated spatial patterns and the magnetic field.

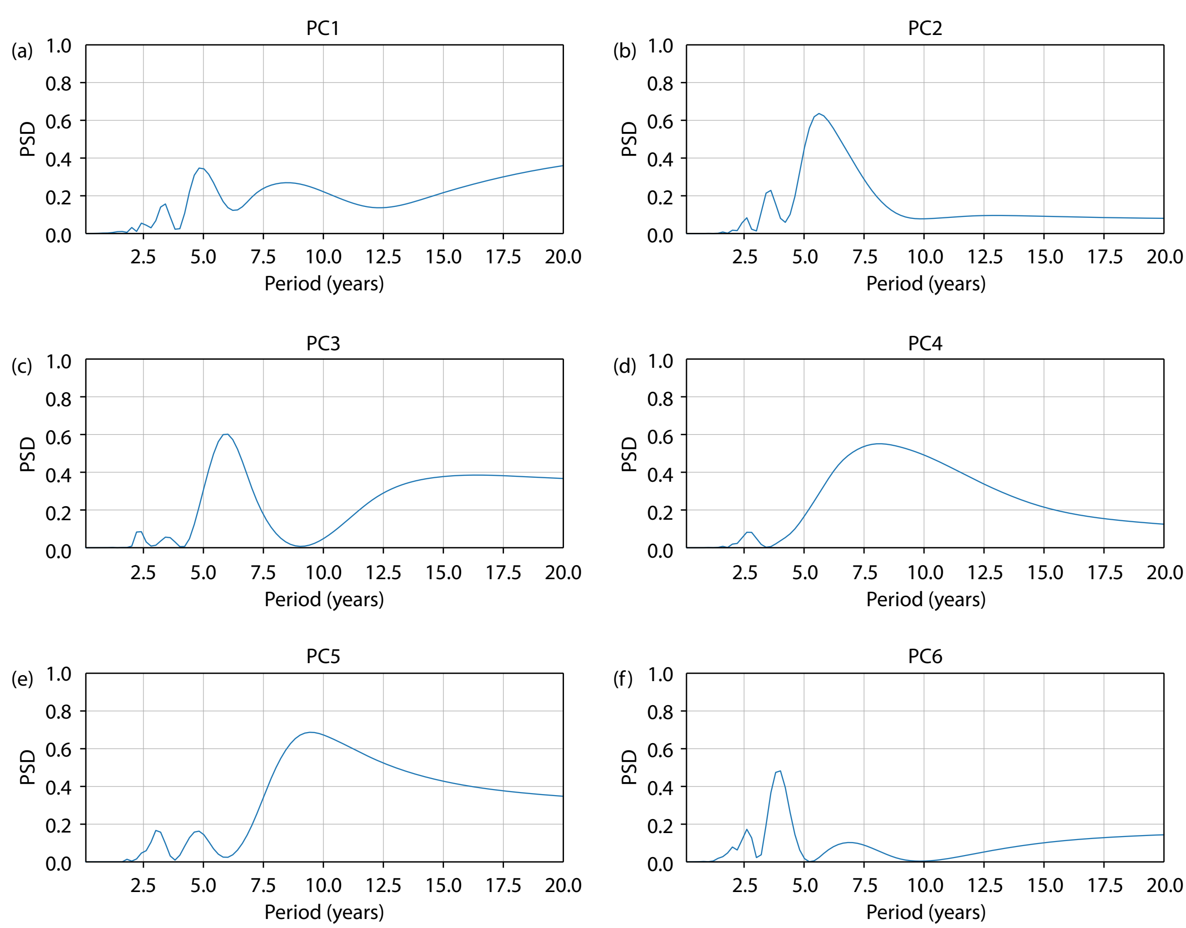

Figure 6. The PSD of each PC of the magnetic field from the ICA.

the characteristic of a rapid linear change after 2013. The significantly correlated regions for this mode correspond to the secular acceleration of the radial component of the core magnetic field in the globe (Figures 2 and 6a). The periodicity of the second mode (Figure 5b) is more distinct. It is dominated by a 5.6-year period. Areas with significant correlations are located mostly in the Atlantic Ocean and the Pacific Ocean. The structure is an east–west-aligned dipole in the Pacific Ocean. The third mode (Figure 5c) also has a distinct periodicity as the second mode, and the peak point is located at the 6-year periodic point (Figure 6c). The signal is mostly active in the western part of the Pacific Ocean and the South American continent. The fourth mode (Figures 5d and 6d) is dominated by an 8.2-year period, with the spatial extent in the Indian Ocean and in the eastern part of the Atlantic Ocean. The fifth mode (Figures 5e and 6e) shows a decadal (9.4-year) period, similar to the fourth mode. This mode is strongly correlated in the eastern part of the Pacific Ocean and the southern part of the Indian Ocean. The sixth mode (Figures 5f and 6f) is dominated by a 4-year period, mostly active in the northern part of the Atlantic Ocean and the southern part of the Pacific Ocean.

4.3 Comparison Analysis of the Gravity and Magnetic Fields

According to the temporal mode signal characteristics corresponding to the six modes in Figure 3, it can be concluded that the first and fourth modes show significant seasonal periodicity. We believe that this periodicity is due to incomplete removal of noncore signals, such as terrestrial hydrological signals and ocean mass variation signals, during the subtraction process. As a result, seasonal periodic signals remain in the gravity residuals. The second, third, fifth, and sixth temporal modes are primarily long-period signals, which may contain characteristic signals from deep

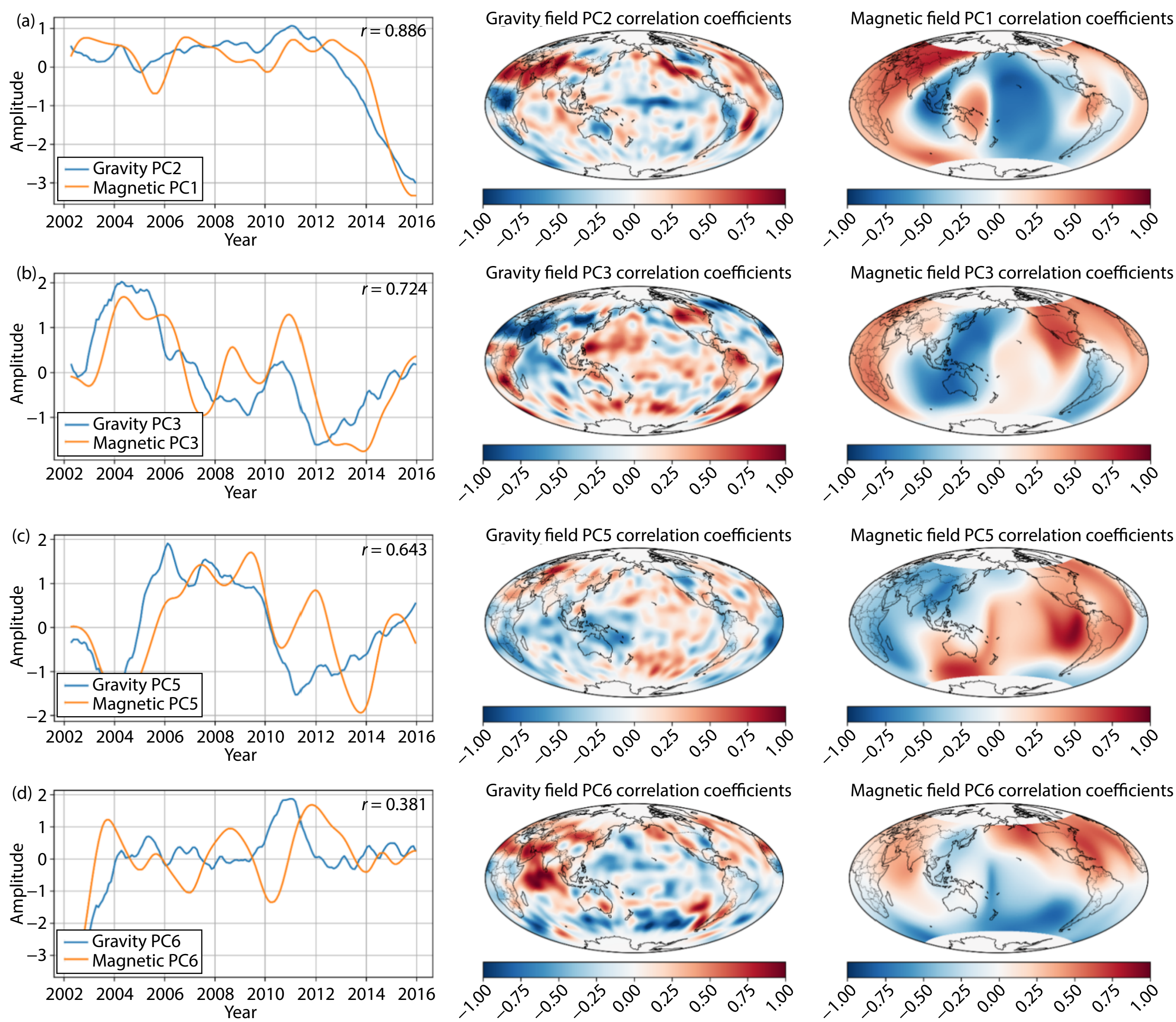

Figure 7. Comparison of the gravity field (blue lines) and the magnetic field (orange lines). (a) Gravity field: PC2; magnetic field: PC1. (b) Gravity field: PC3; magnetic field: PC3. (c) Gravity field: PC5; magnetic field: PC5. (d) Gravity field: PC6; magnetic field: PC6.

in the Earth's interior.

We have compared the four temporal modes of the gravity field with the six temporal modes of the magnetic field one by one. These results are shown in Figure 7. It is obvious that the second temporal mode of the gravity field is significantly correlated with the first mode of the magnetic field (Figure 7a). The correlation coefficient is $r = 0.886$. Both signals were relatively stable before 2012, but after 2012, they both exhibited the characteristic of a rapid linear change, with the magnetic field signal slightly lagging by a few months. Second, the third mode of the gravity field also shows a good correlation with the third mode of the magnetic field ($r = 0.724$; Figure 7b). The periodic characteristics of both signals are quite distinct and similar. Besides the long-period variation, the main periods of the two signals are 5.6 and 6 years, respectively. The correlation between the fifth mode of the gravity field and the fifth mode of the magnetic field is moderate ($r = 0.643$; Figure 7c). The periods of both signals are primarily on a decade scale. Finally, the sixth mode of the gravity field and the sixth mode of the magnetic field show a relatively weak correlation ($r = 0.381$; Figure 7d). The periodic characteristics of the two signals also show a few differences. The dominant period of the gravity signal is 5.2 years, whereas that of the magnetic field is 4 years.

4.4 Field Acceleration Changes Since 2014

Here we focus on the rapidly evolving patterns of field acceleration since 2014. Figure 9 shows an intense magnetic field acceleration in the Pacific region from 2014 to 2017. The structure of the acceleration change is an east–west-aligned dipole in the Pacific region, which corresponds to the results of Finlay et al. (2020). Similar events have been seen at low latitudes below South America and in the Atlantic sector in CHAMP data, which cover the 2000s (Chulliat and Maus, 2014; Finlay et al., 2015). These researchers have selected and computed 60-year-long observatory records from mid to low latitudes spanning from 1960 to 2020. They propose that the rapid acceleration changes observed in the Pacific region should not be viewed as surprising events, but rather that they are parts of the expected secular variation of rapid changes occurring in low-latitude regions (Finlay et al., 2020).

Such rapidly evolving field patterns have also been observed in the second temporal mode of the gravity field. We know that dynamo action in the liquid outer core constitutes the internal source of the core magnetic field. Various researchers have suggested that the dynamic processes of the Earth's deep interior produce a signature in both magnetic and gravity variations (Dumberry and Bloxham, 2004; Dumberry, 2010; Mandea et al., 2012, 2015, 2020; Dumberry and Mandea, 2022). Our results reveal a strong correlation between the gravity field and the radial component of the core magnetic field, particularly the rapid changes observed since 2014 in the second temporal mode of the gravity field and the first temporal mode of the magnetic field (Figure 7). Furthermore, the signal periods of the corresponding temporal modes are relatively similar. Pfeffer et al. (2023) discussed and analyzed a 6-year cycle in the Earth's deep interior and noted that dynamic processes in the fluid outer core observed in the magnetic field may generate changes in the Earth's gravity field. The peak in the PSD of the temporal component of the magnetic field and the gravity field in our study (Figure 8) corresponds to that of Pfeffer et al. (2023). We propose that the processed gravity field signal reflects the mass transfer characteristics of the fluid outer core.

5. Conclusions

In this study, we have computed the gravity field based on the GRACE satellite data and the core magnetic field based on the CHAOS-7 model, with a time span from 2002 to 2016. Publicly available surface hydrological models (introduced in Section 2) have been used to correct the gravity signal to remove noncore signals, such as land hydrology, land glaciers, and ocean mass changes, to separate the gravity field signal containing the mass transfer characteristics of the fluid outer core. The BSS methods have been applied to the gravity field and the magnetic field. After computing the PCs of the first six leading modes, we have

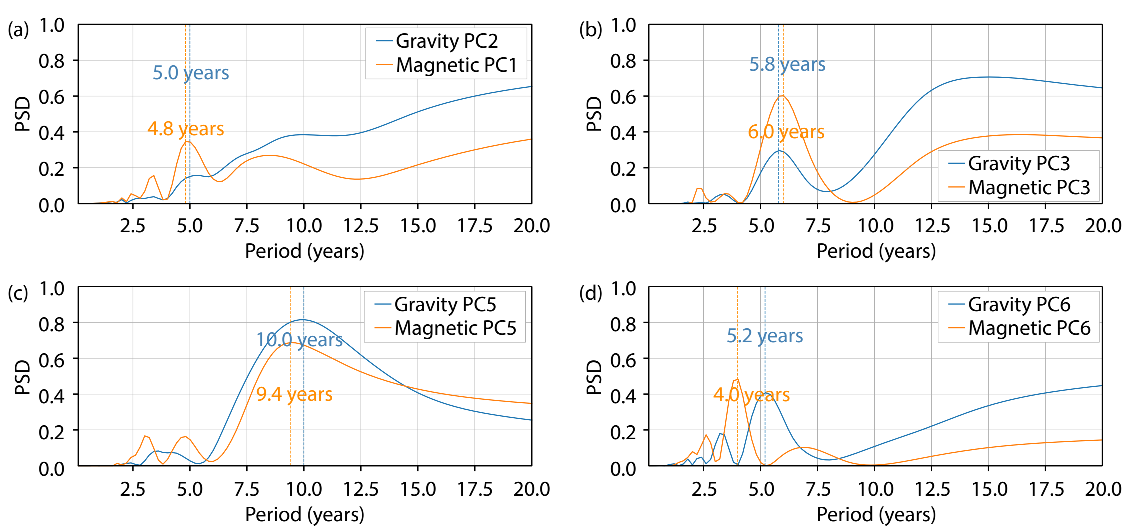

Figure 8. The PSDs of the gravity field (blue line) and the magnetic field (orange line). (a) Gravity field: PC2; magnetic field: PC1. (b) Gravity field: PC3; magnetic field: PC3. (c) Gravity field: PC5; magnetic field: PC5. (d) Gravity field: PC6; magnetic field: PC6.

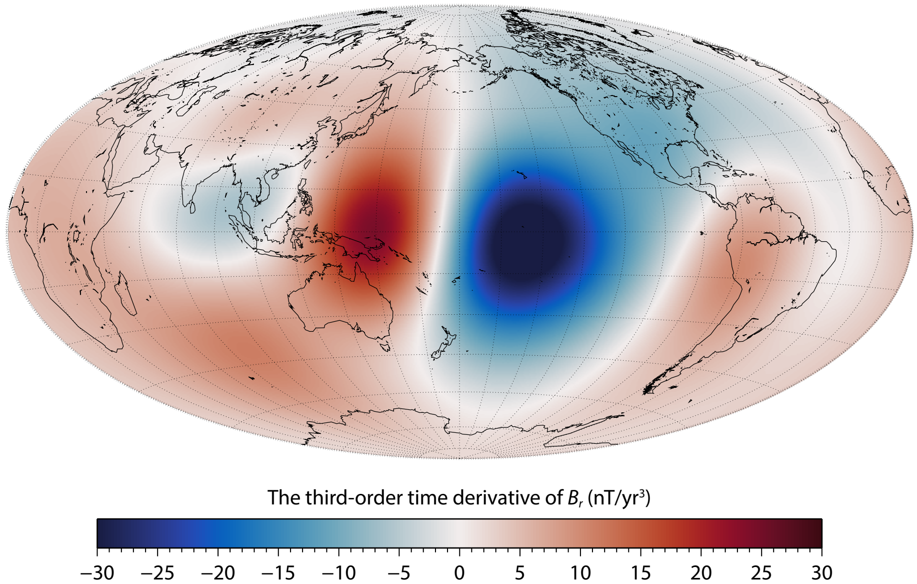

Figure 9. Change in secular acceleration (the third-order time derivative of the radial component of the core magnetic field) from 2014 to 2017. At the Earth's surface after truncation at degree N = 20. The results shown here are taken from the CHAOS-7 model.

analyzed and compared the PCs, which show good correlation, and have calculated the PSD of the time series.

The comparison between the gravity field and magnetic field of mode periods is presented in Figure 8. As expected, the modes with the same term variability are found in the comparison analysis of the gravity and magnetic fields. Significant variations in the gravity field are detected in the 4.6- to 8.6-year period based on GRACE gravity data, which are closely associated with the core magnetic field. We have identified the periodic signals in the first six components of CHAOS-7 radial secular acceleration with considerable power at interannual and decadal time scales. The results in our study are consistent with previous observations and research. According to the results of various researchers, the core processes may contribute to a fraction of the observed gravity field variations, perhaps as much as 10%, which indicates that the mass transfer characteristics of the core may eventually be detectable geodetically. The correlations with the gravity field and the magnetic field may point to a dynamic link between the Earth's deep core mass transfer processes and the global gravity variations. Of course, this possibility will prove successful only if the major surface process contributions are adequately modeled and removed. In this study, although we have attempted to use as many adequate models as possible to remove surface process signals, this remains a challenge because of the uncertainty in the models of these surface processes. We will research how to remove the surface processes more accurately in a future study.

Identifying a distinct influence of core processes in gravity and other geodetic observations would improve the development of the study of core dynamics. From this viewpoint, the survey of the correlations with the gravity field and the magnetic field in our study may provide the foundation for future studies on deep Earth mass changes. Further investigations of how processes of core dynamics influence global mass redistribution and deformation will ultimately enhance our understanding of the Earth's global mass dynamic changes.

Disclosure Statement

No potential conflict of interest was reported by the author(s).

Author Contributions Statement

Y. G. Zhang is the first author. His contributions to our study are collecting all the model data, writing the programs, and finishing the original manuscript. Z. T. Wang is the corresponding author. His contributions to our study are proposing the research ideas and checking the original manuscript. G. H. Ni is one of the authors. His contributions to our study are helping us write the programs and checking the manuscript. S. Z. Zhang is one of the authors. His contributions to our study are helping us collect and process the data.

Data and Code Availability

GRACE data are available from http://www2.csr.utexas.edu/grace. CHAOS-7 models and their updates are available from http://www.spacecenter.dk/files/magnetic-models/CHAOS-7/. GLDAS models are available from https://disc.gsfc.nasa.gov/. ECCO models are available from https://podaac.jpl.nasa.gov/ECCO?sections=data. WOA datasets are available from https://www.ncei.noaa.gov/access/world-ocean-atlas-2018/. RACMO models are available from https://zenodo.org/records/13773130. ICE6G-D models are available from https://www.atmosp.physics.utoronto.ca/~peltier/data.php. The BSS and ICA codes are available from https://www2.iap.fr/users/cardoso/compsep_classic.html.

Acknowledgments

This research was funded by the National Natural Science Foundation of China (Grant Nos. 42274003, 41974007, and 41774019).

References

Bettadpur, S. (2007). Level-2 Gravity Field Product User Handbook. The GRACE

Project (Jet Propulsion Laboratory, Pasadena, CA, 2003). https://www2.csr.utexas.edu/grace/publications/handbook/L2-UserHandbook_v1.0.pdf

Cardoso, J. F. (1999). High-order contrasts for independent component analysis. *Neural Comput.*, *11*(1), 157–192. https://doi.org/10.1162/089976699300016863

Chambers, D. P. (2006). Observing seasonal steric sea level variations with GRACE and satellite altimetry. *J. Geophys. Res.: Oceans*, *111*(C3), C03010. https://doi.org/10.1029/2005JC002914

Chao, B. F., Yu, Y., and Chung, C. H. (2020). Variation of Earth's oblateness J_2 on interannual-to-decadal timescales. *J. Geophys. Res.: Solid Earth*, *125*(6), e2020JB019421. https://doi.org/10.1029/2020JB019421

Chen, J. L., Wilson, C. R., Tapley, B. D., Famiglietti, J. S., and Rodell, M. (2005). Seasonal global mean sea level change from satellite altimeter, GRACE, and geophysical models. *J. Geod.*, *79*(9), 532–539. https://doi.org/10.1007/s00190-005-0005-9

Chen, J. L. (2019). Satellite gravimetry and mass transport in the earth system. *Geod. Geodyn.*, *10*(5), 402–415. https://doi.org/10.1016/j.geog.2018.07.001

Chen, J. L., Wilson, C. R., Kuang, W. J., and Chao, B. F. (2019). Interannual oscillations in earth rotation. *J. Geophys. Res.: Solid Earth*, *124*(12), 13404–13414. https://doi.org/10.1029/2019JB018541

Chulliat, A., and Maus, S. (2014). Geomagnetic secular acceleration, jerks, and a localized standing wave at the core surface from 2000 to 2010. *J. Geophys. Res.: Solid Earth*, *119*(3), 1531–1543. https://doi.org/10.1002/2013JB010604

Dahle, C., Flechtner, F., Gruber, C., König, D., König, R., Michalak, G., and Neumayer, K. H. (2012). GFZ GRACE level-2 processing standards document for level-2 product release 0005. https://icgem.gfz-potsdam.de/docs/L2-GFZ_ProcStds_0005_v1.1-1.pdf

Ding, H., and Chao, B. F. (2018). A 6-year westward rotary motion in the Earth: Detection and possible MICG coupling mechanism. *Earth Planet. Sci. Lett.*, *495*, 50–55. https://doi.org/10.1016/j.epsl.2018.05.009

Dumberry, M., and Bloxham, J. (2004). Variations in the Earth's gravity field caused by torsional oscillations in the core. *Geophys. J. Int.*, *159*(2), 417–434. https://doi.org/10.1111/j.1365-246X.2004.02402.x

Dumberry, M. (2010). Gravity variations induced by core flows. *Geophys. J. Int.*, *180*(2), 635–650. https://doi.org/10.1111/j.1365-246X.2009.04437.x

Dumberry, M., and Mandea, M. (2022). Gravity variations and ground deformations resulting from core dynamics. *Surv. Geophys.*, *43*(1), 5–39. https://doi.org/10.1007/s10712-021-09656-2

Fang, M., Hager, B. H., and Herring, T. A. (1996). Surface deformation caused by pressure changes in the fluid core. *Geophys. Res. Lett.*, *23*(12), 1493–1496. https://doi.org/10.1029/96GL00743

Finlay, C. C., Olsen, N., and Tøffner-Clausen, L. (2015). DTU candidate field models for IGRF-12 and the CHAOS-5 geomagnetic field model. *Earth Planets Space*, *67*(1), 114. https://doi.org/10.1186/s40623-015-0274-3

Finlay, C. C., Kloss, C., Olsen, N., Hammer, M. D., Tøffner-Clausen, L., Grayver, A., and Kuvshinov, A. (2020). The CHAOS-7 geomagnetic field model and observed changes in the South Atlantic Anomaly. *Earth Planets Space*, *72*(1), 156. https://doi.org/10.1186/s40623-020-01252-9

Fok, H. S., and Ma, Z. T. (2021). Characterization of far-field Mekong freshwater mass transport in the southern South China Sea using satellite gravimetry. *Glob. Planet. Change*, *207*, 103686. https://doi.org/10.1016/j.gloplacha.2021.103686

Forget, G., Campin, J. M., Heimbach, P., Hill, C. N., Ponte, R. M., and Wunsch, C. (2015). ECCO version 4: An integrated framework for non-linear inverse modeling and global ocean state estimation. *Geosci. Model Dev.*, *8*(10), 3071–3104. https://doi.org/10.5194/gmd-8-3071-2015

Kusche, J., Eicker, A., and Forootan, E. (2011). Analysis tools for GRACE- and related data sets: Theoretical basis. The International Geoscience Programme (IGCP). IGCP 565: Supporting water resource management with improved Earth observations. http://www.igcp565.org/workshops/Johannesburg_2011/kusche_LectureNotes_analysistools.pdf

Lecomte, H., Rosat, S., Mandea, M., Boy, J. P., and Pfeffer, J. (2023). Uncertainty of low-degree space gravimetry observations: Surface processes versus Earth's core signal. *J. Geophys. Res.: Solid Earth*, *128*(7), e2023JB026503. https://doi.org/10.1029/2023JB026503

Mandea, M., Panet, I., Lesur, V., de Viron, O., Diament, M., and Le Mouël, J. L. (2012). Recent changes of the Earth's core derived from satellite observations of magnetic and gravity fields. *Proc. Natl. Acad. Sci. USA*, *109*(47), 19129–19133. https://doi.org/10.1073/pnas.1207346109

Mandea, M., Narteau, C., Panet, I., and Le Mouël, J. L. (2015). Gravimetric and magnetic anomalies produced by dissolution-crystallization at the core-mantle boundary. *J. Geophys. Res.: Solid Earth*, *120*(9), 5983–6000. https://doi.org/10.1002/2015JB012048

Mandea, M., Dehant, V., and Cazenave, A. (2020). GRACE—Gravity data for understanding the deep Earth's interior. *Remote Sens.*, *12*(24), 4186. https://doi.org/10.3390/rs12244186

Merriam, J. B. (1988). Limits on lateral pressure gradients in the outer core from geodetic observations. *Phys. Earth Planet. Inter.*, *50*(3), 280–290. https://doi.org/10.1016/0031-9201(88)90109-4

Olsen, N., Lühr, H., Sabaka, T. J., Mandea, M., Rother, M., Tøffner-Clausen, L., and Choi, S. (2006). CHAOS—A model of the Earth's magnetic field derived from CHAMP, Ørsted, and SAC-C magnetic satellite data. *Geophys. J. Int.*, *166*(1), 67–75. https://doi.org/10.1111/j.1365-246X.2006.02959.x

Olsen, N., Ravat, D., Finlay, C. C., and Kother, L. K. (2017). LCS-1: A high-resolution global model of the lithospheric magnetic field derived from CHAMP and Swarm satellite observations. *Geophys. J. Int.*, *211*(3), 1461–1477. https://doi.org/10.1093/gji/ggx381

Olsen, N., Albini, G., Bouffard, J., Parrinello, T., and Tøffner-Clausen, L. (2020). Magnetic observations from CryoSat-2: Calibration and processing of satellite platform magnetometer data. *Earth Planets Space*, *72*(1), 48. https://doi.org/10.1186/s40623-020-01171-9

Pfeffer, J., Cazenave, A., Rosat, S., Moreira, L., Mandea, M., Dehant, V., and Coupry, B. (2023). A 6-year cycle in the Earth system. *Glob. Planet. Change*, *229*, 104245. https://doi.org/10.1016/j.gloplacha.2023.104245

Purcell, A., Tregoning, P., and Dehecq, A. (2016). An assessment of the *ICE6G_C(VM5a)* glacial isostatic adjustment model. *J. Geophys. Res.: Solid Earth*, *121*(5), 3939–3950. https://doi.org/10.1002/2015JB012742

Rodell, M., Houser, P. R., Jambor, U., Gottschalck, J., Mitchell, K., Meng, C. J., Arsenault, K., Cosgrove, B., Radakovich, J., … Toll, D. (2004). The global land data assimilation system. *Bull. Amer. Meteor. Soc.*, *85*(3), 381–394. https://doi.org/10.1175/BAMS-85-3-381

Rosat, S., Gillet, N., Boy, J. P., Couhert, A., and Dumberry, M. (2021). Interannual variations of degree 2 from geodetic observations and surface processes. *Geophys. J. Int.*, *225*(1), 200–221. https://doi.org/10.1093/gji/ggaa590

Saraswati, A. T., de Viron, O., and Mandea, M. (2023). Earth's core variability from magnetic and gravity field observations. *Solid Earth*, *14*(12), 1267–1287. https://doi.org/10.5194/se-14-1267-2023

Save, H., Bettadpur, S., and Tapley, B. D. (2016). High-resolution CSR GRACE RL05 mascons. *J. Geophys. Res.: Solid Earth*, *121*(10), 7547–7569. https://doi.org/10.1002/2016JB013007

Swenson, S., and Wahr, J. (2002). Methods for inferring regional surface-mass anomalies from Gravity Recovery and Climate Experiment (GRACE) measurements of time-variable gravity. *J. Geophys. Res.: Solid Earth*, *107*(B9), 2193. https://doi.org/10.1029/2001JB000576

Tapley, B. D., Watkins, M. M., Flechtner, F., Reigber, C., Bettadpur, S., Rodell, M., Sasgen, I., Famiglietti, J. S., Landerer, F. W., … Velicogna, I. (2019). Contributions of GRACE to understanding climate change. *Nat. Clim. Chang.*, *9*(5), 358–369. https://doi.org/10.1038/s41558-019-0456-2

van Dalum, C. T., van de Berg, W. J., Gadde, S. N., van Tiggelen, M., van der Drift, T., van Meijgaard, E., van Ulft, L. H., and van den Broeke, M. R. (2024). First results of the polar regional climate model RACMO2.4. *Cryosphere, 18*(9), 4065–4088. https://doi.org/10.5194/tc-18-4065-2024

VanderPlas, J. T. (2018). Understanding the Lomb–Scargle periodogram. *Astrophys. J. Suppl. Ser.*, *236*(1), 16. https://doi.org/10.3847/1538-4365/aab766

Wahr, J., Molenaar, M., and Bryan, F. (1998). Time variability of the Earth's gravity field: Hydrological and oceanic effects and their possible detection using GRACE. *J. Geophys. Res.: Solid Earth*, *103*(B12), 30205–30229. https://doi.org/10.1029/98JB02844

Wahr, J. M. (2007). Time variable gravity from satellites. In G. Schubert (Ed.), *Treatise on Geophysics* (Vol. 3, pp. 213–237). Amsterdam: Elsevier.

Watkins, A., Fu, Y. N., and Gross, R. (2018). Earth's subdecadal angular momentum balance from deformation and rotation data. *Sci. Rep.*, *8*(1), 13761. https://doi.org/10.1038/s41598-018-32043-8